ADVANCED ELECTRONIC MATERIALS
Open Access
www.advelectronicmat.de

Quantum Transport and Spectroscopy of 2D Perovskite/Graphene Heterostructures

Yan Sun, Corentin Morice, Damien Garrot, Raphael Weil, Kenji Watanabe, Takashi Taniguchi, Miguel Monteverde, and Alexei D. Chepelianskii**

Understanding the quantum transport properties of (Two-dimensional) 2D perovskite heterostructures is key to interpreting their electronic performance and promoting optoelectronic devices. Here, it is shown that clear Shubnikov-de Hass oscillation appears in the heterostructure of monocrystalline 2D perovskites and graphene, thanks to the clean interface. An efficient charge transfer between perovskite nanosheets and graphene is found, facilitating the separation of electrons and holes at the interface. The relation between the charge transfer efficiency and microscopic interface structures is quantitatively described. The evidence of photo-assisted transport from the photo-response of magnetoresistance is revealed, which happens between Landau levels of two graphene layers mediated by hot carriers in the perovskite layer, overcoming the barrier from the organic layers in the Ruddlesden-Popper perovskite phase. These results provide a picture to understand the transport behavior of 2D perovskite/graphene heterostructure and a reference for the controlled design of interfaces in perovskite optoelectronic devices.

1. Introduction

Halide Perovskite is an attractive new class of promising semiconductors for optoelectronic devices.[1,2] To improve the power conversion efficiency and stability, the incorporation of graphene into perovskite-based optoelectronics has been exploited, in which graphene is introduced into transport layers or as electrodes to adjust the optical and electrical properties of perovskite devices.[3–9] Graphene is a monolayer structure of carbon atoms with good optical transparency, excellent stability, high mobility, and outstanding thermal and electrical conductivity.[10–12] Moreover, as an ideal 2D system with a Dirac electronic spectrum, graphene offers a unique platform for discovering novel physics.[13,14]

Ruddlesden- Popper perovskites (RPPs) have recently become appealing candidates in optoelectronic devices, thanks to their improved stability and higher photoluminescence quantum yield, chemical composition and dimensional tunability.[15,16] RPPs have a general formula $LA_2A_{n-1}B_nX_{3n+1}$, where LA and A represent the organic ammonium cations, B is a divalent cation, X is a halide anion, and n is the number of inorganic layers between two planes of LA cations. The large-size organic protective layers in the RPPs enable the natural formation of quantum well structure,[17,18] the integration with other 2D materials,[18–20] and promising wide-range applications.[21–23] However, the interlayer charge transfer hindered by the organic barriers limits the performance of the devices. In this context, graphene has been introduced as a low-resistance contact to form 2D perovskite/graphene field effect transistors owing to the atomically smooth interface and better energy level alignment.[19,24–26] Nevertheless, in graphene-integrated perovskite heterostructures, the microscopic mechanism of electronic properties and interfacial interactions are poorly understood, which obstructs the development of design principles of perovskite devices, partly due to the difficulty of building clear interfaces and keeping phase purity during processing because of the instability of perovskites with humidity and heat.[27] In particular, the perovskite layer's impact on graphene's transport properties has not yet been investigated.

Here, we study quantum transport properties in the heterostructure of molecularly thin perovskite $(BA)_2(MA)_3Pb_4I_{13}$ Ba is $CH_3(CH_2)_3NH_3^+$; Ma is $CH_3NH_3^+$ and monolayer graphene by Shubnikov-de Hass (SdH) oscillation and photoresistance spectroscopy. We report that the perovskite efficiently transfers charges to graphene, leading to a high doping level in graphene

Y. Sun, C. Morice, R. Weil, M. Monteverde, A. D. Chepelianskii
LPS
Université Paris-Saclay
CNRS, UMR 8502, Orsay F-91405, France
E-mail: yan.sun@universite-paris-saclay.fr; alexei.chepelianskii@universite-paris-saclay.fr

D. Garrot
Université Paris-Saclay
UVSQ, CNRS, GEMaC, Versailles 78000, France

K. Watanabe
Research Center for Electronic and Optical Materials
National Institute for Materials Science
1-1 Namiki, Tsukuba 305-0044, Japan

T. Taniguchi
International Center for Materials Nanoarchitectonics
National Institute for Materials Science
1-1 Namiki, Tsukuba 305-0044, Japan

The ORCID identification number(s) for the author(s) of this article can be found under https://doi.org/10.1002/aelm.202400211

DOI: 10.1002/aelm.202400211

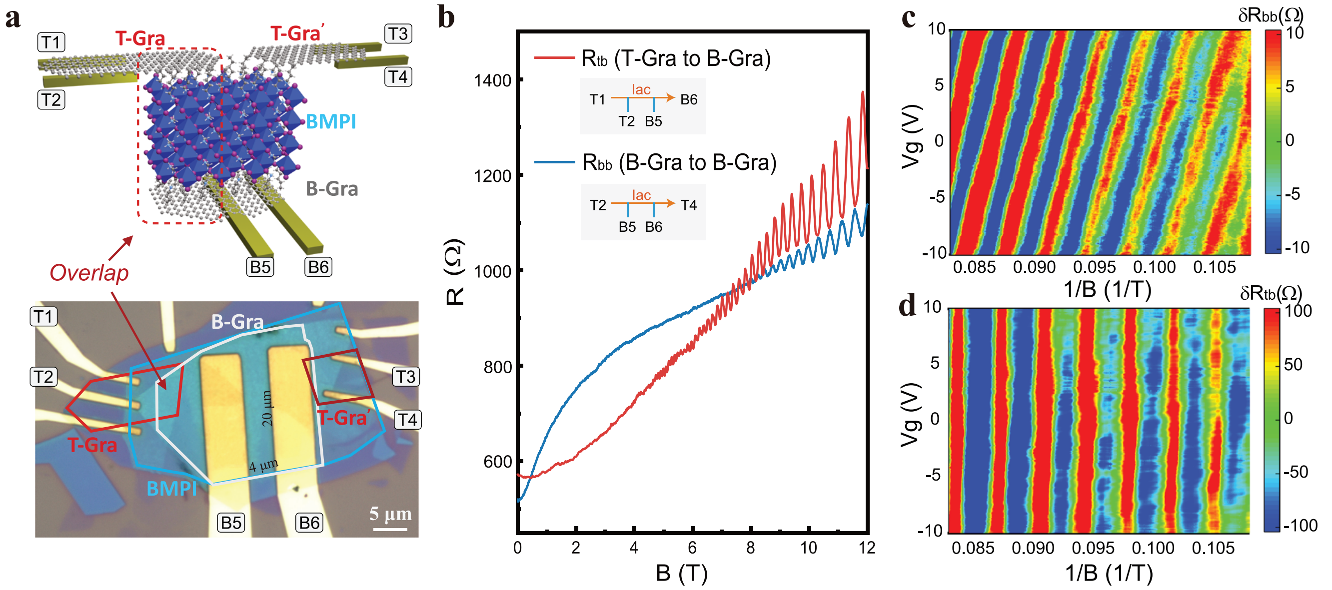

Figure 1. a) Schematic illustration (top) and micrograph (bottom) of a graphene/BMPI/graphene device, where a vertical region is constructed by introducing an overlap from top graphene (T-Gra) to bottom graphene (B-Gra). The whole device is encapsulated by two pieces of BN layers and stacked on a SiO_2/Si substrate, which also works as a bottom gate. The electrodes used in four-terminal connections are labeled. b) The magneto-resistance of BMPI/graphene stack at 1.6 K from B-Gra to B-Gra (R_{bb}) and T-Gra to B-Gra (R_{tb}) contacts with gate bias Vg = 0 V, both of which have the characteristic of the Shubnikov-de Hass (SdH) oscillations. The resistance of R_{bb} is multiplied by 5 (the aspect ratio in device geometry). SdH oscillation as a function of gate bias, c) from R_{bb}, and d) from R_{tb}. In both cases, the graphene is heavily hole-doped with carrier density $n \simeq 2.78 \times 10^{13}$ cm^{-2}, deduced from the oscillation period. c) The SdH in R_{bb} shift with bottom gate voltage V_g indicating hole doping, d) while SdH oscillation in R_{tb} shows a barely visible gate voltage dependence. This is most likely due to the screening of the gate voltage by the bottom graphene.

of up to 2.8×10^{13} cm^{-2}. The clear oscillations indicate locally uniform hole-doping (to within 1%) in graphene from the charge transfer at the interface, rather than ion migration or defects. The density functional theory (DFT) simulations show that the charge transfer efficiency strongly depends on the microscopic structures of the interface, as confirmed by magneto-resistance and micro-fluorescence (micro-PL) experiments. We find that photoresistance in the regime of SdH oscillation provides detailed information on the physics of photo excitations at the graphene-BMPI interface, allowing us to estimate the characteristic lifetimes for photo-gating and heating of the carriers. The photoresistance spectroscopy provides evidence of direct photo-assisted transport between the two graphene contacts through the BMPI layer, indicating that the hot carriers in BMPI interact with both top and bottom graphene.

2. Results and Discussion

2.1. Transport Devices of 2D Perovskite/Graphene

$(BA)_2(MA)_3Pb_4I_{13}$ (BMPI) crystal is prepared by temperature-controlled crystallization. The clean periodic diffraction peaks in the X-ray diffraction (XRD) pattern in Figure S1 (Supporting Information) confirm the phase purity of those 2D perovskite crystals. Since generally perovskite is sensitive to heat and humidity, developing a method to avoid degradation during fabrication is crucial. To minimize heating, the 2D perovskite is assembled by resist-free dry transfer, so that the transfer temperature remains lower than 60 °C. To verify the quality of the BMPI layer after the exfoliation and dry-transfer process, we performed micro-PL microscopy on a pristine BN/graphene/BMPI/BN sample. As shown in Figure S2 (Supporting Information, The mean photoluminescence intensity of BMPI/graphene is almost half as large as that of BMPI. A quenching of BMPI PL by graphene is expected since graphene has no bandgap and is rendered as a collector for both electrons and holes, which is also proof of a clean interface between BMPI and graphene.[28] All the above characterization results show that our crystals and fabrication technique, including exfoliation and dry transfer, ensure a good sample quality, making transport measurements possible. A schematic and optical image of a graphene-BMPI device used in transport experiments is shown in **Figure** 1a. The device containing both horizontal and vertical stacking regions is constructed by transferring the BMPI flake (around four layers, thickness about 14 nm) on top of a graphene layer, followed by partly covering the stack with another small piece of graphene. The device is encapsulated with two h-boron nitride layers. The details of materials and device fabrication can be found in the methods section.

We investigate transport from top to bottom graphene through BMPI as well as the conductivity of the bottom graphene covered by the BMPI layer. Four-terminal electrical contacts are used to eliminate the contact resistance and resistance from wires. The resistance of the bottom graphene, R_{bb}, is normalized by the geometrical aspect ratio (five squares). The resistance from top to bottom graphene, R_{tb}, is measured from the region T-Gra (top graphene) to B-Gra (bottom graphene) (Figure 1a). The bottom graphene was measured at room temperature before deposition of the BMPI layers and exhibits a sharp Dirac peak and a small electron doping (Figure S3, Supporting Information). After stacking with BMPI, the Dirac peak strongly shifted, possibly indicating the charge transfer process, which has been seen in graphene-based Van der Waals heterostructures.[29–31] To confirm and quantify the charge transfer in the device, we cooled the sample to 1.6 K. The resistance of the samples decreased only weakly ≈ 15% during cooling (Figure S3, Supporting Information) for transport from top to bottom graphene. This indicates that the BMPI is sufficiently conducting even at low temperature and that transport through BMPI is not thermally activated confirming that we prepared clean graphene/BMPI interfaces. In the following, we present magneto-transport to elucidate the nature of the possible charge transfer process between graphene and BMPI, and photoresistance spectroscopy to probe the interaction between photo-excitations in BMPI and transport in graphene.

2.2. Magneto-Transport at the Graphene-Perovskite Interface

Figure 1b shows periodic oscillation on the magnetoresistance, with four-terminal contacts on R_{bb} (blue) and R_{tb} (red) at 1.6 K. The oscillation originates from the SdH effect, which is related to the crossing between the Fermi level and quantized Landau Levels (LL). The appearance of SdH oscillation in this hybrid graphene/perovskite system under an intermediate field (<8 Tesla) implies that the interface between graphene and BMPI is clean. According to Lifshitz-Kosevich theory, the SdH oscillations in the magnetoresistance of two-dimensional electron gas systems can be described approximately by Equation (1).[32,33] In the limit of small SdH, their amplitude δR is given by:

$$\delta R = R_0 D_T \exp\left(-\frac{\pi}{\mu B}\right)\cos\left(\pi\frac{hn}{2eB}\right) \tag{1}$$

here n is the carrier density, μ is the carrier mobility, and R_0 is the mean longitudinal resistance around which magneto-resistance oscillates. The phase of the oscillation takes into account the Berry phase π for graphene.[34] The temperature damping is described by the D_T:

$$D_T = \frac{2\pi^2 k_b T/\hbar\omega_c}{\sinh(2\pi^2 k_b T/\hbar\omega_c)} \tag{2}$$

where $\omega_c = eB/m_c^*$ is cyclotron frequency, and $m_c^* = \hbar k_F/v_F$ is the effective mass (cyclotron mass).[35]

The resistance versus 1/B measured with gate voltage ranging from –10 V to 10 V displays a Landau fan diagram (Figure 1c). Applying Equation (1), the oscillation pattern for R_{bb} (Figure 1c) and R_{tb} connections (Figure 1d) are simulated (Figure S4, Supporting Information). We find that in both cases, the graphene is heavily hole-doped, with density $n \simeq 2.78 \times 10^{13}$ cm^{-2} at $Vg =$ 0 V. This doping level is so high that the hole density is about 1% of the areal density of carbon atoms in graphene (which is about ≈ 3.8×10^{15} cm^{-2}).The typical distance between two holes is around 2 nm in the graphene, while the carbon-carbon bond length in graphene is around 0.14 nm, and the lattice constant of BMPI is around 0.87 nm.[36,37] We notice that similar doping levels have been reported in graphene-RuCl$_3$ heterostructures.[38,39] We note that the bottom-gate voltage required to reach this carrier density is around 400V, which is beyond the breakdown limit of the gate voltage. Considering the non-equivalent fabrication process for top and bottom graphenes, the nearly equivalent doping level in both layers suggests that the high hole density in graphene is independent of the fabrication process, but an intrinsic property of BMPI/graphene hybrids. The peaks of SdH oscillations shift and the period slightly increases in R_{bb} when increasing the gate voltage, as expected in quantitative agreement with the change in hole density. For R_{tb}, we find that bottom gate voltage has little infuence on the resistance, this is probably related to the screen effect by the bottom graphene and a dominating contribution of the top graphene/BMPI interface due to the electrode geometry (Supporting Information).

Since graphene becomes hole doped due to charge transfer with the perovskite, the 14nm thick BMPI layer becomes electron doped with the same surface carrier density. The resistance between top and bottom graphenes seems largely due to in plane graphene transport as evidenced by the SdH oscillations. This allows us to find a lower limit on the electron mobility inside BMPI layer. We find than for mobility $\geqslant 10^{-2}$ cm^2 V^{-1} s^{-1}, the vertial BMPI resistance to becomes much smaller than the resistance from in plane graphene transport.

Figure 2a shows that the amplitude of SdH oscillations, δR_{bb}, gradually decreases with increasing temperature, and tends to disappear under sufficiently high temperature (>54.5 K), where δR_{bb} is calculated by subtracting the resistance with a liner fit to the background. The temperature-dependent SdH oscillations are fitted with Equation (1). From the amplitude of the oscillation peaks at various temperatures, the only fitting parameter m_c^* is available from the relation between the amplitude and T/B by Equation (2),[40] which gives $m_c^* = 0.08\ m_e$ (Figure 2b). While through $m_c^* = \hbar k_F/v_F = \hbar\sqrt{\pi n}/v_F$,[35] the theoretical effective mass $m_c^* = 0.12\ m_e$, where m_e is the electron mass, and the Fermi velocity v_F is around 1×10^6 m s^{-1},[41] as shown in Figure 2b with a broken line for comparison. The detailed discussion on effective mass and mobility in the heterostructure is in Supporting Information.

2.3. Interfacial Terminations Affect the Charge Transfer Process

In addition to quantum oscillations, the magneto-resistance in Figure 1b shows a global positive magneto-resistance trend, which is not expected in a single carrier Drude model. We simulated the potential distribution in the sample by the finite element method (FEM) and modeled the conductivity of our sample as the sum of two conductivities corresponding to the weakly/highly doped regions. We find that this two-region model can reproduce the overall magneto-resistance trend (Figure 2c). The high-doped region gives the saturating high field mobility, while the low-doping region of $n_1 \approx 1.26 \times 10^{12}$ cm^{-2} with higher mobility of $\mu_1 \approx 11\,000$ cm^{-2} V^{-1} s^{-1} explains the low field magnetoresistance. Evidence of the co-existence of regions with different carrier densities is also found in the micro-PL microscopy on the pristine BN/graphene/BMPI/BN sample, where we see inhomogeneous photoluminescence with domain size around 2 μm^2 (Figure S2, Supporting Information).

To find out the correlation between the charge transfer process and the microscopic structure of the BMPI/graphene

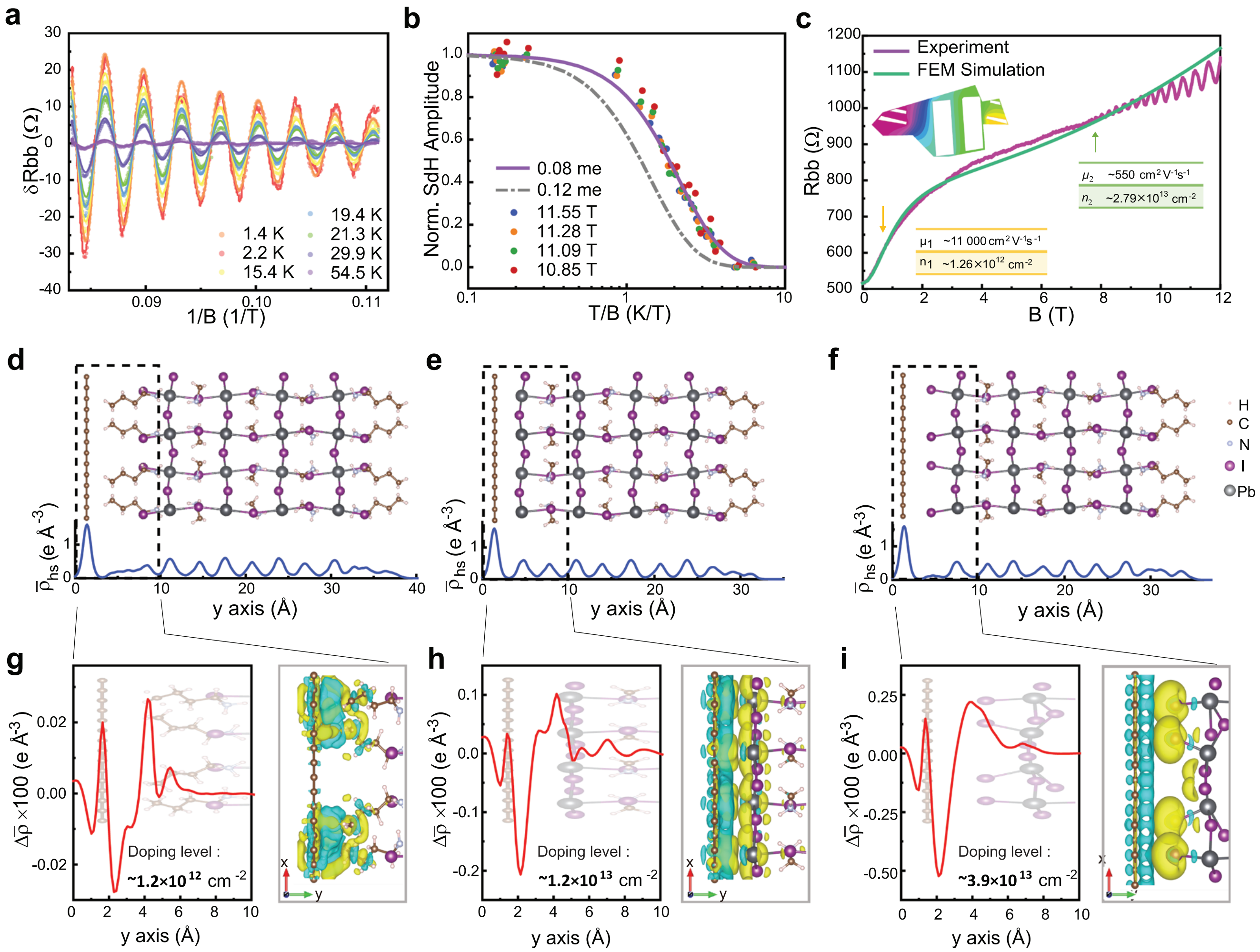

Figure 2. a) Temperature-dependent SdH oscillations which are fitted with Equation (1). b) The normalized amplitudes of the oscillations as a function of T/B are collected under several oscillation peaks labeled by the magnetic field, from which the m_c^* is available through Equation (2). c) Simulations of magneto-resistance of R_{bb} with a model of two types of carriers with different mobility. The mobilities and doping levels are shown in the tables. The simulated voltage drop on a model geometry from the finite element method under 12 T is shown in the inset as an example. DFT simulation of the electron density at the interface between BMPI and graphene for different perovskite terminations. d) BA molecules, e) Pb-I, f) Iodide ions. The blue curves denote the plane-averaged integral charge density along the stacking direction (y-axis) in the graphene/BMPI heterostructure ($\bar{\rho}_{\text{hs}}$) with each type of interface. The charge transfer process mainly happens at the interface and is revealed by calculating the plane-averaged differential charge density ($\Delta\bar{\rho}$). Positive (negative) values in $\Delta\bar{\rho}$ indicate charge accumulation (depletion). In (g–i), the $\Delta\bar{\rho}$ (red line, multiplied by 100) zoomed at the interface shows that the electrons are lost on the graphene side while accumulating on the BMPI side. With BA molecular as the termination (g), a slight charge transfer corresponds to moderate hole doping in graphene. Whereas in the case of the Pb-I section (h) or I ions (i) as termination, a drastic transfer happens on the interface and results in an order of magnitude higher doping in graphene. The doping level of graphene in each case is labeled. The image (right-hand side) shows the atomic structure of the interface for each case and the color-coded density contours of $\Delta\rho$ from the x-y plane, the yellow (cyan) regions correspond to $\Delta\rho > 0$ ($\Delta\rho < 0$).

interface, we considered three structure models of the interface, with the following possible terminations of BMPI: BA molecule (Figure 2d), Pb-I (Figure 2e), and iodine (Figure 2f). The charge densities in graphene are calculated using DFT and compared with the experiment. Because of the charge transfer process, the charge density in the heterostructure (ρ_{hs}) is not equal to the charge densities for non-interacting graphene(ρ_{graphene}) and BMPI(ρ_{BMPI}). To show the charge carriers distribution, a differential charge density $\Delta\rho$ is calculated from $\Delta\rho = \rho_{\text{hs}} - \rho_{\text{graphene}} - \rho_{\text{BMPI}}$. We introduce the plane-averaged differential charge density $\Delta\bar{\rho}$, defined as the stacking plane-average of $\Delta\rho$, to estimate the magnitude of charge transfer,

$$\Delta\bar{\rho} = \frac{1}{S_g}\int \Delta\rho \, dxdz \tag{3}$$

The y coordinate is the stacking direction and x, z are the coordinates within the graphene plane. The integral runs over slices of the unit cell for a fixed y, and S_g is the graphene surface within the unit cell that is used for normalization. The plane-averaged integral charge density of the graphene/BMPI heterostructure ($\bar{\rho}_{\text{hs}}$)

is shown along the y-axis (blue line), which corresponds very well to each crystal structure.

The charge transfer primarily arises at the interface between BMPI and graphene, as illustrated in Figure 2g,h,i, where $\Delta\rho$ is concentrated. Positive values of $\Delta\bar{\rho}$ indicate electron accumulation, while the negative values represent electron depletion. For all the simulated interfaces, electrons are transferred from the graphene to BMPI, leading to hole-doped graphene. The amplitude of this doping strongly depends on the type of termination. The density contours on the right-hand side visually reflect the differential charge density distribution in the x-y plane zoomed on the interface.

In Figure 2g, only a small value of $\Delta\bar{\rho}$ can be seen in the charge transfer from the BA molecular termination. This mild charge transfer corresponds to a doping level of around 1.2×10^{12} cm^{-2} in graphene, which is close to the average density in the low doping region as estimated from magnetoresistance in Figure 2c. In contrast, with the Pb-I termination (Figure 2h), the doping level increases by an order of magnitude, reaching up to 1.2×10^{13} cm^{-3} (see Section S3, Supporting Information for details). For this termination, the separation of charge accumulation and depletion layers becomes visible from the density contours of $\Delta\rho$. Finally in the case of I^- termination (Figure 2i), a considerable amount of charges accumulate around I^-, and results in doping of 3.9×10^{13} cm^{-2} in the graphene layer. We note that the density observed from the Shubnikov-de Haas oscillations is between these two high doping values. In the experiment, only a single SdH oscillation period is visible, which suggests only one type of high doping interface being realized in the experiment with a low enough disorder to exhibit quantum oscillations. From the differential charge density, we estimate that the charge transfer creates an electric field of more than 10^7 Vcm^{-1}. This large electric field can facilitate the separation of electrons and holes at the graphene/BMPI interface or be used for avalanche-carrier multiplication devices.

2.4. Photoresistance Spectrum on SdH Oscillation

For highly doped graphene in our sample, the mean spacing between holes (around 2 nm) is comparable to the exciton Bohr radius which is estimated to be about 1 nm in 2D RPPs and 4.2 nm in 3D perovskites.[42–44] This implies the possibility of a strong interaction between carriers in graphene and excitons hosted by BMPI.[45,46] To study photo-physics directly at the BMPI-graphene interfaces, we performed photoresistance measurements using a home-built cryogenic probe in which the sample was immersed in superfluid helium to ensure good thermalization under photo-excitation down to 1.6 K. A sketch of the experimental setup is shown in **Figure** 3a. The sample was biased with both AC and DC currents, and two lock-in amplifiers were used to measure sample resistance(R, from AC current and with frequency f_{ac}), as well as the photoresistance at the chopper frequency (R^p, from DC current and with f_p). Since the heterojunctions are highly doped, the photo response was always a small change in the total sample resistance.

We started by illuminating the sample with a 532 nm laser. The photoresistance from B-Gra to B-Gra, R^p_{bb}, and from T-Gra to B-Gra, R^p_{tb}, are shown in Figure 3b together with the corresponding sample resistance δR_{bb} and δR_{tb}, in which we see photoresistance oscillations in the SdH region. The strongest photoresistance appeared at high magnetic field in the SdH region, which can be attributed to a change in the carrier density (photo-gating) and the heating of graphene carriers.[47,48] The out-of-phase component of photoresistance (with respect to SdH) allows us to estimate the relative photo-induced change in the carrier density to be $\Delta n/n \simeq 2.5 \times 10^{-5}$. The in-phase photoresistance gives a carrier temperature increase of 0.3 K, which is consistent with the heating expected from our laser excitation intensity. A typical lifetime τ for electrons transferred from BMPI to graphene is around 400 ns. Details are given in Section S4 (Supporting Information).

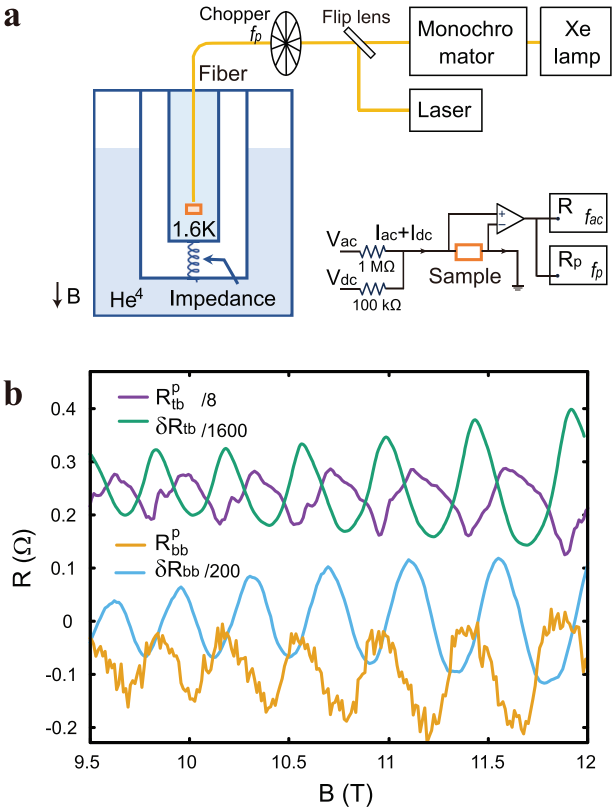

Figure 3. a) Schematic of the setup for the photo-excitation transport measurement, in which the illumination is laser or a Xenon lamp followed by a monochromator. The sample is immersed into superfluid helium four to accelerate thermal dissipation. The photoresistance is synchronized at chopper frequency (f_p) and biased by DC current. b) Photoresistance at high magnetic field in SdH region for the connection of B-Gra to B-Gra (R^p_{bb}) and T-Gra to B-Gra (R^p_{tb}), compared to the corresponding amplitude of SdH oscillation δR_{bb} and δR_{tb}. The δR_{tb} and R^p_{tb} are shifted for clarity. The excitation is from 532 nm laser with the power of 40 Wm^{-2}. The R^p_{tb} shows more asymmetrical oscillations, while R^p_{bb} with weak phase shift from δR_{bb} due to the combination of photo-gating and heating.

In contrast to the simply phase-shifted SdH signal in R^p_{bb}, R^p_{tb} oscillates very anharmonic with pronounced negative peaks and some signatures of beating between two periods (Figure 3b). This difference can be related to the difference between photocurrent (extraction of photo-excited electron-hole pairs from the BMPI) and photo-assisted transport (transfer of carriers between the two graphenes through excitation of BMPI)

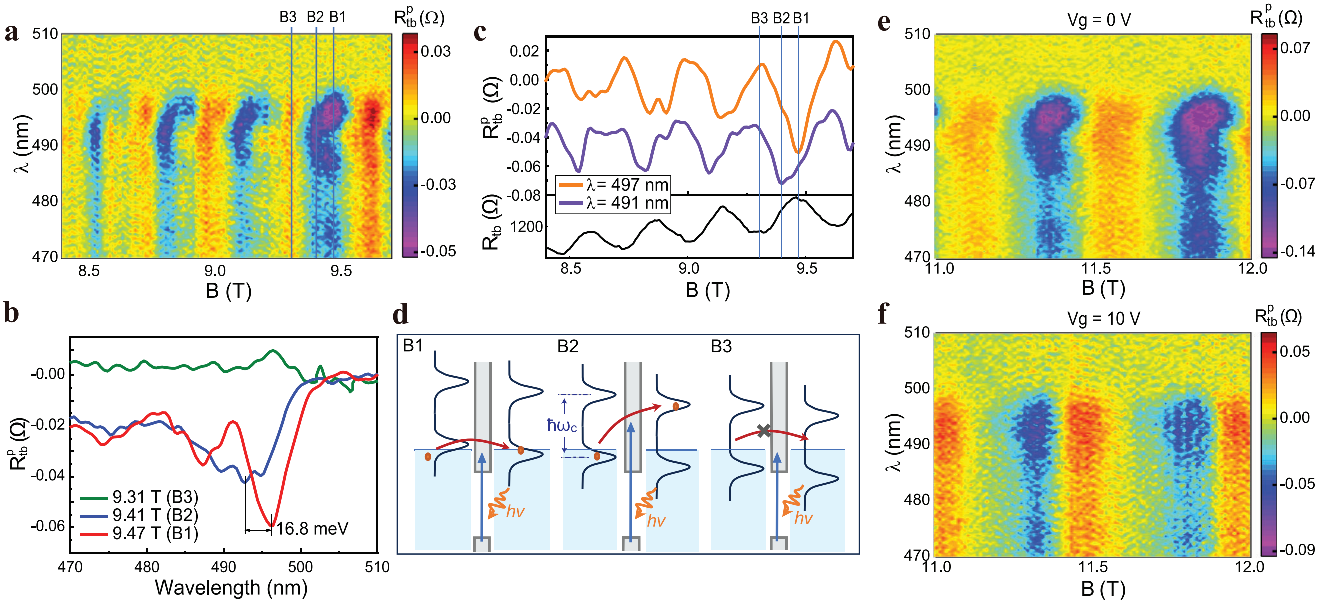

Figure 4. a) The change in resistance under illumination (R^p_{tb}) from R_{tb} is plotted versus excitation wavelength on the vertical axis and magnetic field B on the horizontal axis. The numbers 1,2,3 label magnetic fields of 9.47 T (B_1), 9.41 T (B_2), and 9.31 T (B_3) respectively in one period. b) Photoresistance spectra show a shift of the absorption peak appearing from B_1 to B_2. The shift wavelength corresponds to an energy of 16 meV. c) Magnetic field dependence of the R^p_{tb} show an enhanced amplitude at the maximum of R_{tb} (the minimum of R^p_{tb}) compared to the amplitude expected from harmonic oscillations. d) A sketch of a qualitative model for photoresistance. For B_1 the Fermi energy lies inside the LL for both top and bottom graphenes, this gives maximal photoassisted transport. For B_2 the Fermi energy enters the gap between LL in one of the graphene layers, photo-assisted transport now requires an extra LL spacing energy $\hbar\omega_c$ to reach the first empty LL. This extra energy blue shifts the photoresistance spectrum at B_2 compared to B_1 and the observed shift of 16 meV is indeed comparable to $\hbar\omega_c \simeq 14$ meV. Finally, for B_3, the Fermi energy lies in the gap between LL for both graphenes leading to a suppressed photoresistance. Panels e) and f) show the comparison of photoresistance peaks under $V_g = 0$ V and f) $V_g = 10$ V. The spectral shift disappears with gate voltage. Since both BMPI and the top graphene are screened from V_g by the bottom graphene, the gate voltage only changes the carrier density in the bottom graphene demonstrating that near alignment of the LL between top to bottom graphene is indeed required.

processes, which are allowed in two graphene-contacts geometry, but are absent in the single bottom-graphene geometry. Our sample is symmetric between top and bottom graphene and the applied DC voltages between top/bottom graphene are small (1 mV), thus strong photocurrent is not expected, leaving photo-assisted transport as the most likely explanation for the strongly anharmonic photoresistance. We note that in control experiments with a pristine graphene device, no measurable photoresistance spectrum is found under the same conditions.

To understand the mechanism of photo-assisted transport in the heterostructure, we focused on R^p_{tb} for the photoresistance spectroscopy experiments, in which a monochromator-filtered Xe-lamp is used as excitation light. As shown in **Figure** 4a,b,c, at B1 = 9.47 T, a photoresistance peak is observed around 497 nm, with a weak photoresistance tail at longer wavelengths. The signal at 532 nm is no longer visible because of the much weaker excitation intensity from the Xenon lamp after filtering of the excitation wavelength through the monochromator. As the magnetic field increases to B2 = 9.41 T, a red-shift of the main absorption peak becomes visible at maxima of SdH for R_{tb}, disappearing rapidly away from the maximum. In Figure 4b we show that this shift in photoresistance spectra appears at field $B_1 = 9.47$ T, but disappears already for $B_2 = 9.41$ T. The shift in wavelength of the photoresistance spectrum corresponds to an energy of around ΔE = 16 meV, with the spacing between LL of around 14 meV, and a change of LL energy of around $\hbar e(B_1 - B_2)/m^*_c = 0.09$ meV from field B_1 to B_2. The spectral shift ΔE is thus much closer to the total LL spacing, suggesting that it does not come from a single graphene layer but instead from photo-induced transport between the top and bottom graphenes.

A sketch of our qualitative model for photoresistance is shown in Figure 4d. When no gate voltage is applied, the density of the top and bottom graphene are almost identical. Thus at SdH maxima, direct photo-assisted transport between the two incompletely filled LL is allowed (process 1). The photon energy is then absorbed within the BMPI layer enabling charge transfer between the two graphenes. In this situation the magnetic field dependence of the R^p_{tb} starts to show an enhanced amplitude at SdH maxima compared to harmonic SdH oscillations (see R^p_{tb} at 497 nm in Figure 4c), leading to the more anharmonic magnetic field dependence that was also seen with 532 nm laser excitation. As the magnetic field is changed slightly the LL in one of the two graphenes goes below the Fermi energy and an extra energy must be provided to transfer carriers to the first empty LL, requiring an increase in photon energy by the LL spacing $\hbar\omega_c$ (process 2). Finally, when LL on both graphenes are full at SdH minima the photoassisted transport is suppressed leading to weak photoresistance (process 3).

In this scenario, the LL alignment between the two graphenes is important. We compared the signal at $V_g = 0$ V (Figure 4e) and $V_g = 10$V (Figure 4f), corresponding to a different position of the Fermi energy concerning LL in graphenes. The gate voltage mainly changes the density of the bottom graphene and is screened in the rest of the device. with $V_g = 10$V, the shift of the spectrum with the magnetic field disappears completely, which is in agreement with our model.

The anharmonic photoresistance SdH oscillations and the energy associated with the spectral shift close to $\hbar\omega_c$ confirm our qualitative model for photo-assisted transport relying on the alignment of the LL between the two graphenes. This model implicitly assumes hot-carrier transport in BMPI, as the relative energy of the LL in both graphenes would not matter if carriers have to hop through many sites with random energies on the way. This may explain the blue-shifted onset for the main photoresistance spectrum starting at around 500 nm (≈2.48 eV) compared to the expected position of the optical absorption spectrum for $n = 4$ BMPI, which is reported with bandgap of 2.07 eV.[19] The extra energy would then correspond to the excitation of higher-energy hot carriers in the BMPI layer.

3. Conclusion

Through SdH oscillations in low-temperature magneto-transport, we reveal a strong charge transfer process at the BMPI/graphene interface, leading to a hole doping in graphene. We show that the charge transfer significantly depends on the termination of the perovskite at its interface by DFT calculation, which is in agreement with magneto-resistance and micro-PL microscopy. The photoresistance at a high magnetic field in the regime of SdH oscillations is investigated, where the graphene LL becomes quantized. A phase shift appears on the photoresistance under laser excitation, as the combined effects of the photo-gating effect and slight rise of carrier temperature. From the spectroscopy, the onset of photoresistance shift by an energy similar to the LL spacing in graphene, suggests photo-assisted transport between the two graphene contacts through hot carriers in BMPI.

Our results show that perovskite/graphene heterostructure enables the exploration of new regimes in photo-assisted transport, and a possible access to new fundamental physics as the interface homogeneity improves in future devices. The strong built-in electric field associated with the efficient charge transfer can facilitate the separation of electrons and holes at the graphene/BMPI interface. Combined with the high hole mobility in graphene, this heterostructure gives the hope of highly efficient optoelectronic devices.

4. Experimental Section

Synthesis of BMPI Crystals: The synthesis of the BMPI single crystals was adapted from ref. [18]. Generally, 154mg of PbO (0.69 M), 34mg of BAI (0.17 M), and 82 mg of MAI (0.52 M) precursors were mixed in a vial with 0.884 ml HI and 0.116 ml H_3PO_2 solvent. The PbO can be substituted by the same molar amount of PbI_2. A clear yellow solution is obtained after heating and stirring at 110 °C for one hour. The stock solution was slowly cooled to room temperature at a rate of 1 °Ch^{-1} in an oven. The precipitated black crystals were vacuum filtered and rinsed with toluene several times, followed by drying in a vacuum overnight. The photoluminescence spectrum of the bulk crystal and monolayer BMPI shows a single narrow peak at around 664 nm (Figure S1, Supporting Information).

Fabrication of Graphene/BMPI/Graphene Device: Au(30 nm)/Ti(5 nm) electrodes were deposited on a thin layer of flat hexagonal boron nitride (bottom BN), which had been transferred on a doped silicon substrate with a 300 nm-thick oxide layer. Then a monolayer graphene flake (bottom graphene) was transferred on top of electrodes and BN, and annealed under 200 °C at 1×10^{-5} mbar for 2 h. Polydimethylsiloxane (PDMS) is used during mechanical exfoliation of BMPI flake (Figure S1). A BMPI flake on the PDMS surface was transferred to fully cover the bottom graphene. During resist-free dry-transfer, 60 °C heating was used for a short time (around 1 min) to help release the BMPI pieces. Afterward, two top-graphene flakes were picked up at room temperature with a big top BN flake supported by PDMS. When stamping the top graphene/BN layer, we introduced a small overlap region between the top and the bottom graphene through BMPI layer. The exfoliation and dry-transfer processes were implemented in the air. The stack is encapsulated between two BN layers (Top-BN and Bottom-BN). The electrodes conducting the top and bottom graphene were fabricated on top of the bottom-BN layer before transferring graphene and BMPI, to avoid heating of the BMPI and contamination of the graphene surface during electrode fabrication. The bottom graphene electrodes are wider for better adhesion of the electrodes on the bottom BN layer and to ensure continuity across the bottom BN step.The long aspect ratio of the bottom electrodes was chosen to have a well-defined geometry to measure bottom graphene conductivity with a large contact area between graphene and electrodes. For top graphene contacts that lay flat on the silicon surface, thinner electrodes were used and the geometry was adapted to the shape of the top graphene flakes. The device is placed on a highly doped silicon wafer with 280 nm SiO_2, which also act as a gate electrode.

Transport Measurements: Transport measurements are performed using SR830 lock-in amplifiers at an AC bias current of 100 nA, and a low-noise amplifier (LI-75A) with 100x Gain. The frequency for magnetoresistance is 17 Hz (f_{ac} in Figure 3a), and for photoresistance is 39 Hz (f_p) synchronized with the chopper frequency. Low-pass π filters were added to each measuring line to protect the sample from noise and abrupt voltage discharges during connection switching. photoresistance measurements are performed in a pumped superfluid He4 chamber (temperature around 1.6 K). Helium flux into the chamber is fixed by an impedance with a room-temperature flow rate of around 3.5×10^{-2} mbar L s^{-1}.

First-Principles Computational Methods: The charge density calculations in this work are based on density functional theory (DFT) conducted with plane-wave basis set and projector augmented wave (PAW) pseudopotentials implemented in the Quantum Espresso (QE).[49,50] The exchange-correlation function is taken as the Perdew–Burke–Ernzerhof (PBE) type of the generalized gradient approximation(GGA).[51] DFT-d correction is used for all calculations to describe the van der Waals force between BMPI and graphene.[52] To simulate the 2D system and eliminate the interaction effects between the adjacent layers, the calculations were implemented with a vacuum thickness of 25 Å. The cell parameters and atomic positions are fully relaxed with the k-point mesh of $3 \times 1 \times 6$, generated by using the Monk-horst–Pack scheme. A kinetic energy cut-off of 550 eV is adopted for plane-wave expansion, and the convergence tolerances for the energy and force are set at 10^{-8} eV. We used a Gaussian smearing with a deviation of 0.01 Ha. All the parameters were tested for convergence.

Supporting Information

Supporting Information is available from the Wiley Online Library or from the author.

Acknowledgements

The work was financially supported by funding from ANR-20-CE92-0041 (MARS), IDF- DIM SIRTEQ, and the European Research Council (ERC) under the European Union's Horizon 2020 research and innovation programme (grant Ballistop agreement no. 833350). The authors thank S.

Guéron, Z.Y.Chen, and E. Delporte for the discussions on the physical process. The authors also thank M. Entin for the help on modeling.

Conflict of Interest

The authors declare no conflict of interest.

Author Contributions

Y.S., M.M., and A.C. designed the experiments and implemented the magneto-transport measurements. Y.S. fabricated the devices used for the study and performed calculations of electron charge density under the guidance of C.M. D.G. carried out micro-PL measurements. R.W contributes to the technical assistance. K.W. and T.T. provide boron nitride crystals used in the experiment. A.C. and Y.S. implemented the Finite element method. All authors discussed the results and contributed to the writing of the paper.

Data Availability Statement

The data that support the findings of this study are available from the corresponding author upon reasonable request.

Keywords

charge transfer, hot-carriers, magnetoresistance, perovskite heterostructure, photoassisted transport

Received: March 12, 2024
Revised: June 24, 2024
Published online: September 3, 2024

---

[1] M. Jeong, I. W. Choi, E. M. Go, Y. Cho, M. Kim, B. Lee, S. Jeong, Y. Jo, H. W. Choi, J. Lee, J.-H. Bae, S. K. Kwak, D. S. Kim, C. Yang, *Science* **2020**, *369*, 1615.
[2] A. Fakharuddin, M. K. Gangishetty, M. Abdi-Jalebi, S.-H. Chin, A. R. bin Mohd Yusoff, D. N. Congreve, W. Tress, F. Deschler, M. Vasilopoulou, H. J. Bolink, *Nat. Electron.* **2022**, *5*, 203.
[3] S. Pescetelli, A. Agresti, G. Viskadouros, S. Razza, K. Rogdakis, I. Kalogerakis, E. Spiliarotis, E. Leonardi, P. Mariani, L. Sorbello, M. Pierro, C. Cornaro, S. Bellani, L. Najafi, B. Martiń-Garciá, A. E. D. R. Castillo, R. Oropesa-Nun ez, M. Prato, S. Maranghi, M. L. Parisi, A. Sinicropi, R. Basosi, F. Bonaccorso, E. Kymakis, *Nat. Energy* **2022**, *7*, 597.
[4] C. Petridis, G. Kakavelakis, E. Kymakis, *Energy Environ. Sci.* **2018**, *11*, 1030.
[5] A. Agresti, S. Pescetelli, A. L. Palma, B. Martín-García, L. Najafi, S. Bellani, I. Moreels, M. Prato, F. Bonaccorso, A. Di Carlo, *ACS Energy Lett.* **2019**, *4*, 1862.
[6] B. Taheri, N. Y. Nia, A. Agresti, S. Pescetelli, C. Ciceroni, A. E. D. R. Castillo, L. Cinà, S. Bellani, F. Bonaccorso, A. Di Carlo, *2D Mater.* **2018**, *5*, 045034.
[7] S. Razza, S. Pescetelli, A. Agresti, A. Di Carlo, *Energies* **2021**, *14*, 1069.
[8] Y. Lee, J. Kwon, E. Hwang, C.-H. Ra, W. J. Yoo, J.-H. Ahn, J. H. Park, J. H. Cho, *Adv. Mater.* **2015**, *27*, 41.
[9] H.-C. Cheng, G. Wang, D. Li, Q. He, A. Yin, Y. Liu, H. Wu, M. Ding, Y. Huang, X. Duan, *Nano Lett.* **2016**, *16*, 367.
[10] R. R. Nair, P. Blake, A. N. Grigorenko, K. S. Novoselov, T. J. Booth, T. Stauber, N. M. Peres, A. K. Geim, *science* **2008**, *320*, 1308.
[11] C. R. Dean, A. F. Young, I. Meric, C. Lee, L. Wang, S. Sorgenfrei, K. Watanabe, T. Taniguchi, P. Kim, K. L. Shepard, J. Hone, *Nat. Nanotechnol.* **2010**, *5*, 722.
[12] A. K. Geim, K. S. Novoselov, *Nat. Mater.* **2007**, *6*, 183.
[13] K. S. Novoselov, A. K. Geim, S. V. Morozov, D.-e. Jiang, Y. Zhang, S. V. Dubonos, I. V. Grigorieva, A. A. Firsov, *science* **2004**, *306*, 666.
[14] K. S. Novoselov, A. K. Geim, S. V. Morozov, D. Jiang, M. I. Katsnelson, I. V. Grigorieva, S. Dubonos, A. Firsov, *nature* **2005**, *438*, 197.
[15] E. Shi, Y. Gao, B. P. Finkenauer, A. H. Coffey, L. Dou, *Chem. Soc. Rev.* **2018**, *47*, 6046.
[16] K. Leng, W. Fu, Y. Liu, M. Chhowalla, K. P. Loh, *Nat. Rev. Mater.* **2020**, *5*, 482.
[17] N. Wang, L. Cheng, R. Ge, S. Zhang, Y. Miao, W. Zou, C. Yi, Y. Sun, Y. Cao, R. Yang, Y. Wei, Q. Guo, Y. Ke, M. Yu, Y. Jin, Y. Liu, Q. Ding, D. Di, L. Yang, G. Xing, H. Tian, C. Jin, F. Gao, R. H. Friend, J. Wang, W. Huang, *Nat. Photonics* **2016**, *10*, 699.
[18] K. Leng, I. Abdelwahab, I. Verzhbitskiy, M. Telychko, L. Chu, W. Fu, X. Chi, N. Guo, Z. Chen, Z. Chen, Z. Chen, C. Zhang, Q.-H. Xu, J. Lu, M. Chhowalla, G. Eda, K. P. Loh, *Nat. Mater.* **2018**, *17*, 908.
[19] K. Leng, L. Wang, Y. Shao, I. Abdelwahab, G. Grinblat, I. Verzhbitskiy, R. Li, Y. Cai, X. Chi, W. Fu, P. Song, A. Rusydi, G. Eda, S. A. Maier, K. P. Lohet, *Nat. Commun.* **2020**, *11*, 5483.
[20] D. Pan, Y. Fu, N. Spitha, Y. Zhao, C. R. Roy, D. J. Morrow, D. D. Kohler, J. C. Wright, S. Jin, *Nat. Nanotechnol.* **2021**, *16*, 159.
[21] A. Liu, H. Zhu, S. Bai, Y. Reo, M. Caironi, A. Petrozza, L. Dou, Y.-Y. Noh, *Nat. Electron.* **2023**, *6*, 559.
[22] B.-S. Qiao, S.-Y. Wang, Z.-H. Zhang, Z.-D. Lian, Z.-Y. Zheng, Z.-P. Wei, L. Li, K. W. Ng, S.-P. Wang, Z.-B. Liu, *Adv. Mater.* **2023**, *35*, 2300632.
[23] B. Zhang, T. Zheng, J. You, C. Ma, Y. Liu, L. Zhang, J. Xi, G. Dong, M. Liu, S. Liu, *Adv. Mater.* **2023**, *35*, 2208875.
[24] Y. Shao, Y. Liu, X. Chen, C. Chen, I. Sarpkaya, Z. Chen, Y. Fang, J. Kong, K. Watanabe, T. Taniguchi, A. Taylor, J. Huang, F. Xia, *Nano Lett.* **2017**, *17*, 7330.
[25] Z. Tan, Y. Wu, H. Hong, J. Yin, J. Zhang, L. Lin, M. Wang, X. Sun, L. Sun, Y. Huang, K. Liu, Z. Liu, H. Peng, *J. Am. Chem. Soc.* **2016**, *138*, 16612.
[26] L. Qiu, G. Si, X. Bao, J. Liu, M. Guan, Y. Wu, X. Qi, G. Xing, Z. Dai, Q. Bao, G. Li, *Chem. Soc. Rev.* **2023**, *52*, 212.
[27] M. Sheng, X. Chang, X. Mao, Y. Gao, X. Xuan, H. Xie, H. Mu, Y. Niu, S. Gong, M. Qian, *Adv. Electron. Mater.* **2024**, *2300842*, https://onlinelibrary.wiley.com/doi/full/10.1002/aelm.202300842.
[28] L. Niu, X. Liu, C. Cong, C. Wu, D. Wu, T. R. Chang, H. Wang, Q. Zeng, J. Zhou, X. Wang, W. Fu, P. Yu, Q. Fu, S. Najmaei, Z. Zhang, B. I. Yakobson, B. K. Tay, W. Zhou, H. T. Jeng, H. Lin, T. C. Sum, C. Jin, H. He, T. Yu, Z. Liu, *Adv. Mater.* **2015**, *27*, 7800.
[29] M. Sup Choi, G.-H. Lee, Y.-J. Yu, D.-Y. Lee, S. Hwan Lee, P. Kim, J. Hone, W. Jong Yoo, *Nat. Commun.* **2013**, *4*, 1624.
[30] L. Britnell, R. Gorbachev, R. Jalil, B. Belle, F. Schedin, A. Mishchenko, T. Georgiou, M. Katsnelson, L. Eaves, S. V. Morozov, N. M. R. Peres, J. Leist, A. K. Geim, K. S. Novoselov, L. A. Ponomarenko, *Science* **2012**, *335*, 947.
[31] J.-H. Chen, C. Jang, S. Xiao, M. Ishigami, M. S. Fuhrer, *Nat. Nanotechnol.* **2008**, *3*, 206.
[32] P. Coleridge, R. Stoner, R. Fletcher, *Phys. Rev. B* **1989**, *39*, 1120.
[33] A. Fujita, *Glob. J. Sci. Front. Res.* **2014**, *14*.
[34] Y. Zhang, Y.-W. Tan, H. L. Stormer, P. Kim, *nature* **2005**, *438*, 201.
[35] A. C. Neto, F. Guinea, N. M. Peres, K. S. Novoselov, A. K. Geim, *Rev. Mod. Phys.* **2009**, *81*, 109.
[36] D. R. Cooper, B. D'Anjou, N. Ghattamaneni, B. Harack, M. Hilke, A. Horth, N. Majlis, M. Massicotte, L. Vandsburger, E. Whiteway, V. Yu, *Int. Scholarly Res. Not.* **2012**, *2012*, 501686.

[37] Y. Shao, W. Gao, H. Yan, R. Li, I. Abdelwahab, X. Chi, L. Rogée, L. Zhuang, W. Fu, S. P. Lau, S. F. Yu, Y. Cai, K. P. Loh, K. Leng, *Nat. Commun.* **2022**, *13*, 138.
[38] S. Mashhadi, Y. Kim, J. Kim, D. Weber, T. Taniguchi, K. Watanabe, N. Park, B. Lotsch, J. H. Smet, M. Burghard, K. Kern, *Nano Lett.* **2019**, *19*, 4659.
[39] B. Zhou, J. Balgley, P. Lampen-Kelley, J.-Q. Yan, D. G. Mandrus, E. A. Henriksen, *Phys. Rev. B* **2019**, *100*, 165426.
[40] M. Monteverde, C. Ojeda-Aristizabal, R. Weil, K. Bennaceur, M. Ferrier, S. Guéron, C. Glattli, H. Bouchiat, J. Fuchs, D. Maslov, *Phys. Rev. Lett.* **2010**, *104*, 126801.
[41] D. Elias, R. Gorbachev, A. Mayorov, S. Morozov, A. Zhukov, P. Blake, L. Ponomarenko, I. Grigorieva, K. Novoselov, F. Guinea, et al., *Nat. Phys.* **2011**, *7*, 701.
[42] J.-C. Blancon, A. V. Stier, H. Tsai, W. Nie, C. C. Stoumpos, B. Traore, L. Pedesseau, M. Kepenekian, F. Katsutani, G. Noe, J. Kono, S. Tretiak, S. A. Crooker, C. Katan, M. G. Kanatzidis, J. J. Crochet, J. Even, A. D. Mohite, *Nat. Commun.* **2018**, *9*, 2254.
[43] A. Miyata, A. Mitioglu, P. Plochocka, O. Portugall, J. T.-W. Wang, S. D. Stranks, H. J. Snaith, R. J. Nicholas, *Nat. Phys.* **2015**, *11*, 582.
[44] A. Konzelmann, B. Frank, H. Giessen, *J. Phys. B: At., Mol. Opt. Phys.* **2019**, *53*, 024001.
[45] L. Wang, S. Papadopoulos, F. Iyikanat, J. Zhang, J. Huang, T. Taniguchi, K. Watanabe, M. Calame, M. L. Perrin, F. J. García de Abajo, et al., *Nat. Mater.* **2023**, *22*, 1094.
[46] K. K. Paul, J.-H. Kim, Y. H. Lee, *Nat. Rev. Phys.* **2021**, *3*, 178.
[47] L. Ju, J. Velasco, E. Huang, S. Kahn, C. Nosiglia, H.-Z. Tsai, W. Yang, T. Taniguchi, K. Watanabe, Y. Zhang, G. Zhang, M. Crommie, A. Zettl, F. Wang, *Nat. Nanotechnol.* **2014**, *9*, 348.
[48] F. Luo, M. Zhu, H. Sun, W. Luo, G. Peng, Z. Zhu, X.-A. Zhang, S. Qin, et al., *AIP Adv.* **2018**, *8*, 11.
[49] P. Giannozzi, S. Baroni, N. Bonini, M. Calandra, R. Car, C. Cavazzoni, D. Ceresoli, G. L. Chiarotti, M. Cococcioni, I. Dabo, A. D. Corso, S. d. Gironcoli, S. Fabris, G. Fratesi, R. Gebauer, U. Gerstmann, C. Gougoussis, A. Kokalj, M. Lazzeri, L. Martin-Samos, N. Marzari, F. Mauri, R. Mazzarello, S. Paolini, A. Pasquarello, L. Paulatto, C. Sbraccia, S. Scandolo, G. Sclauzero, A. P. Seitsonen, et al., *J. Phys.: Condens. Matter* **2009**, *21*, 395502.
[50] P. Giannozzi, O. Andreussi, T. Brumme, O. Bunau, M. B. Nardelli, M. Calandra, R. Car, C. Cavazzoni, D. Ceresoli, M. Cococcioni, et al., *J. Phys.: Condens. Matter* **2017**, *29*, 465901.
[51] J. P. Perdew, K. Burke, M. Ernzerhof, *Phys. Rev. Lett.* **1996**, *77*, 3865.
[52] V. Barone, M. Casarin, D. Forrer, M. Pavone, M. Sambi, A. Vittadini, *J. Comput. Chem.* **2009**, *30*, 934.